ACS APPLIED MATERIALS & INTERFACES

www.acsami.org

Research Article

Ultrathin Fe–ReS_2 Nanosheets as Electrocatalysts for Accelerating Sulfur Reduction in Li–S Batteries

Jianli Tang, Chunqiao Jin, Liuxiang Huo, Shenyu Du, Xionghu Xu, Yuting Yan, Kai Jiang, Liyan Shang,* Jinzhong Zhang, Yawei Li, Zhigao Hu,* and Junhao Chu

Cite This: *ACS Appl. Mater. Interfaces* 2022, 14, 50870–50879

Read Online

ACCESS | Metrics & More | Article Recommendations | Supporting Information

ABSTRACT: Lithium–sulfur batteries are promising next-generation energy storage systems with high theoretical specific capacity. Despite extensive research efforts, it is still challenging to rationally design electrocatalysts with fast kinetics and effective adsorption of polysulfides. Herein, Fe-doped ReS_2 (Fe–ReS_2) ultrathin nanosheets are prepared as an electrocatalyst to trap the intermediates and accelerate the sulfur reduction reaction kinetics. Density functional theory calculations combined with activation energies in the multistep sulfur reduction reaction reveal that the Fe–ReS_2 considerably reduces the activation energy and optimizes the optimum adsorption strength of polysulfides and catalytic activity. The Fe–ReS_2/S exhibits a highly reversible discharge capacity of 882.3 mA h g^{-1} at 1 C. For 500 cycles, the capacity fade rate is 0.013% per cycle. Moreover, in situ Raman spectroscopy measurements further confirmed that both sulfur reduction and oxidation processes were significantly enhanced by Fe–ReS_2.

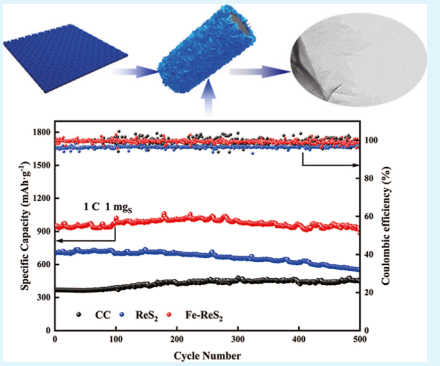

KEYWORDS: *electrocatalyst, Fe-doped ReS_2, ultrathin nanosheets, sulfur reduction, Li–S batteries*

Downloaded via EAST CHINA NORMAL UNIV on November 20, 2022 at 12:14:30 (UTC).
See https://pubs.acs.org/sharingguidelines for options on how to legitimately share published articles.

1. INTRODUCTION

Lithium–sulfur (Li–S) batteries are regarded as prospective energy storage devices due to their ultrahigh theoretical specific capacity of 1675 mA h g^{-1}.[1−14] Nevertheless, the commercialization of Li–S batteries is still hindered by the low electronic/ionic conductivity of sulfur species and the notorious shuttling effect of LiPSs.[15−17] Most significantly, the reaction kinetics of soluble intermediate products to the insoluble final products is sluggish, resulting in the accumulation of LiPSs in the electrolyte. This is the main origin of the shuttling effect.[18−20] To overcome this drawback, an electrocatalytic approach is required to accelerate reversible conversion between LiPSs and Li_2S. Therefore, reasonable design of electrocatalysts will mitigate the shuttle effect and improve their rate capability.

Recently, various two-dimensional (2D) transition-metal dichalcogenides (TMDs) including WS_2,[21,22] $MoTe_2$,[23] MoS_2,[24−28] and ReS_2[29−32] have been developed as electrocatalysts and polar hosts to improve the performance of Li–S batteries.[32−34] In order to accelerate the conversion kinetics of LiPS and resist the shuttle effect to a certain extent, these electrocatalysts are designed.[24,35,36] However, the poor electrical conductivity and limited active sites caused by uncontrollability over the thickness of TMDs electrocatalysts will give rise to a decrease in cycling stability. Although the concept of electrocatalysts has been proposed in recent reports, the fundamental catalytic mechanism in the sulfur reduction reaction is still rarely researched.

WS_2[21,22] faces lamina propria stacking, thus reducing the number of exposed active sites. It also limits the conductivity between S–W–S. Although 1T-MoS_2 has many active sites on the edge and in the plane, 1T is metastable and easily transformed into a stable 2H state, resulting in a large reduction of catalytic active centers.[24−28] Compared with other TMD materials (such as WS_2 and MoS_2),[21,22,24−28] ReS_2 has very weak interlayer coupling. As a result, the reactant diffuses to its deep space to achieve a better catalytic process. The energy level of ReS_2 can be well adjusted by doping engineering so as to improve the charge density around low-valence cations. Low-valent Fe domains contribute to providing more active sites for chemisorption. However, there are still few reports on the application of low-price transition-metal-doped ReS_2 nanosheets in lithium–sulfur batteries. Unlike other 2D TMDs, ReS_2 has a direct band gap (1.47–1.61 eV)[37] and it exhibits a naturally twisted trigonal lattice octahedron (1T) structure. Its unique structure and anisotropy endow it with unique characteristics and excellent electrocatalytic activity, for example, hydrogen evolution reaction.[38,39] These properties demonstrate its potential as an effective electrocatalyst for LiPS transformation.

Received: August 9, 2022
Accepted: October 26, 2022
Published: November 7, 2022

© 2022 American Chemical Society

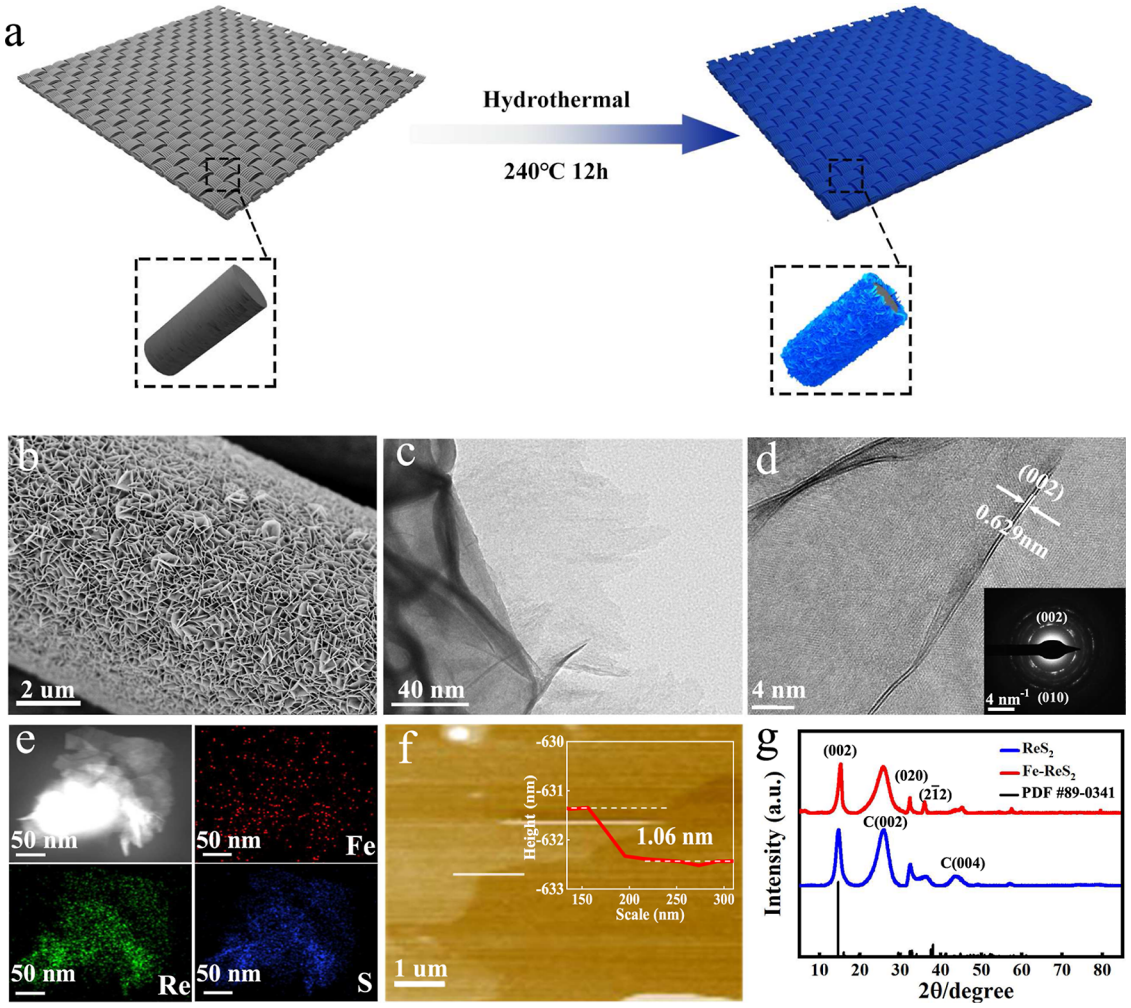

Figure 1. Growth of interconnected Fe-doped ReS_2 nanosheet arrays on CC fibers and morphological characterization. (a) Schematic illustration of preparation of the Fe-doped ReS_2/CC. (The cathode material for the battery is prepared by a simple one-pot hydrothermal method.) (b) SEM image of Fe−ReS_2/CC. (c) TEM image of Fe−ReS_2 nanosheets. (d) High-resolution TEM image of Fe−ReS_2 nanosheets. Lower right corner of (d) is the SAED pattern of the Fe−ReS_2. (e) Corresponding element mapping of Fe−ReS_2 nanosheets. (f) AFM image of Fe−ReS_2 nanosheets. (g) XRD patterns of ReS_2/CC and Fe−ReS_2/CC.

Trace transition-metal doping in atomically ordered ReS_2 nanosheets, especially in the low domain (e.g., Fe^{3+}, Fe^{2+}, etc.),[40] can disturb the lattice, thus exposing more electrocatalytically active sites.[52] To our knowledge, Fe-doped ReS_2/carbon cloth composites have not been reported in Li−S batteries so far. Therefore, it is urgent to design and prepare a new Fe-doped ReS_2/carbon fabric matrix reasonably and reveal the adsorption and catalytic mechanism of Fe-doped ReS_2 on LiPSs.

Herein, we present the design of Fe-doped ReS_2[29−31,52] (denoted as Fe−ReS_2) 2D ultrathin nanosheets to strengthen the adsorption and conversion of LiPSs, mitigating the shuttling effect.[41] In situ-grown Fe−ReS_2 ultrathin nanosheets possess good conductivity and abundant active catalysis sites, ensuring that the electrocatalyst exhibits superior reaction kinetics.[42,43] Theoretical calculation results confirm that Fe−ReS_2 effectively enhances the absorptivity of LiPSs and electrocatalytic activity toward LiPS conversion. The electrocatalysis mechanism of the sulfur reduction reaction is further revealed by in situ Raman spectroscopy. Consequently, the cell with Fe−ReS_2 ultrathin nanosheets exhibits excellent cycling stability of more than 500 cycles with a low capacity fading rate of 0.013% per cycle at 1 C.

2. EXPERIMENTAL SECTION

2.1. Preparation of ReS_2 and Fe−ReS_2. First, a carbon cloth (CC, 1.5 cm × 1.3 cm) was ultrasonically cleaned with acetone, ethanol, and deionized water. To obtain Fe−ReS_2/CC, 0.238 mmol ammonium perrhenate (Sigma-Aldrich, ≥99%), 0.5 mmol hydroxylamine hydrochloride (ADAMAS-BETA, ≥99%), and 0.5 mmol thiourea (J&K, AR, 99%) were added into 10 mL of deionized water and stirred with magnetic force for 30 min. Subsequently, 0.074 mmol iron(III) chloride hexahydrate was added into 5 mL of deionized water under magnetic stirring for 30 min. The above two solutions were mixed and continue stirring for 30 min under a magnetic stirrer to form a mixed solution. The CC was soaked in the mixed solution and placed in 25 mL of polytetrafluoroethylene lining. Then, the whole stainless-steel autoclave was kept at 240 °C for 24 h. After cooling it to room temperature, the product was collected. The product was washed three times with deionized water and ethanol, respectively. Then, it was dried at 60 °C overnight under vacuum. For comparison, ReS_2 was prepared under the same conditions without adding iron(III) chloride hexahydrate.

2.2. Preparation of ReS_2/CC/S and Fe−ReS_2/CC/S. Sulfur powder and lithium sulfide (Li_2S) were mixed in a certain molar ratio. Then, a certain amount of 1,2-dimethoxymethane/1,3-dioxolane solution (DME/DOL, v/v = 1/1) was added. It was stirred continuously overnight in an argon glovebox to synthesize the required Li_2S_8 solution. After configuring the Li_2S_8 solution into 0.3 M, 13 μL of

https://doi.org/10.1021/acsami.2c14282
ACS Appl. Mater. Interfaces 2022, 14, 50870−50879

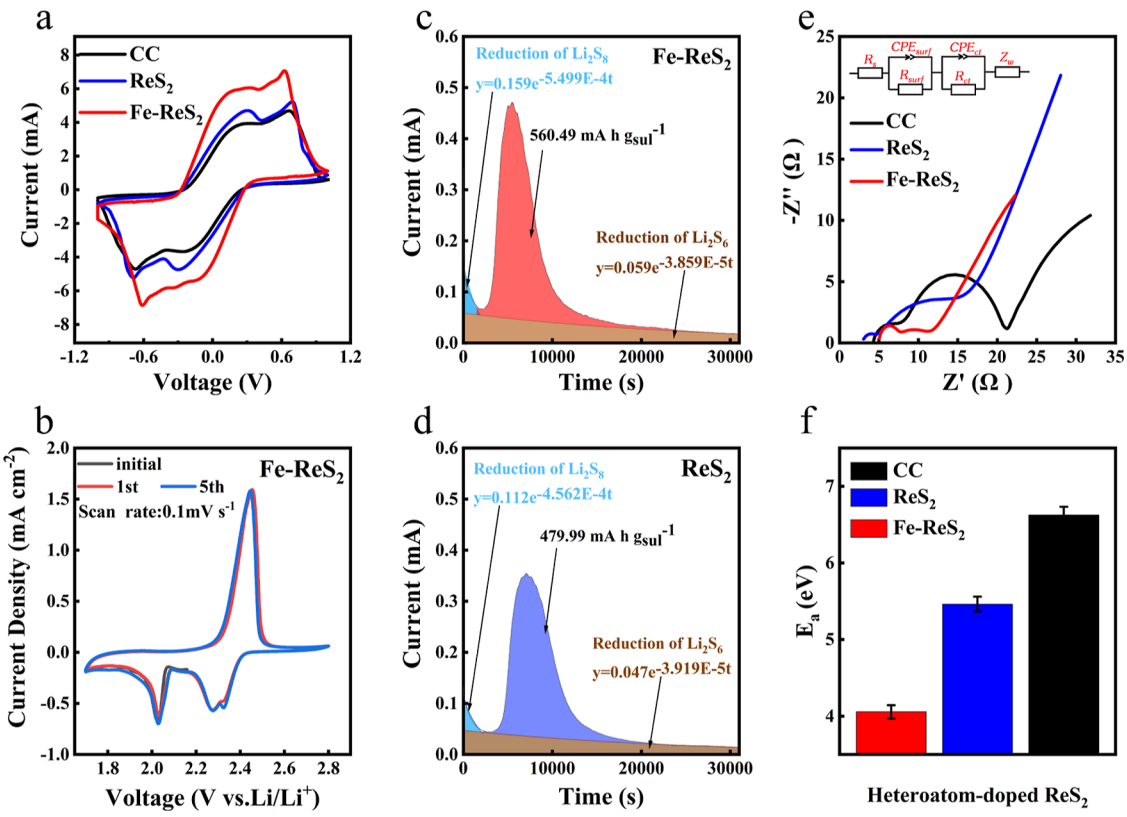

Figure 2. (a) CV curve of the Li_2S_6 symmetrical battery with CC, ReS_2, and Fe−ReS_2 load at a scanning rate of 1 mV s^{-1}. (b) Fe−ReS_2 full battery stability CV graph. (c) Potentiostatic discharge curves of Fe−ReS_2. (d) Potentiostatic discharge curves of ReS_2. (e) EIS profile of CC, ReS_2, and Fe−ReS_2 electrodes at 25 °C. (f) SRR activation energy of different active substances at the initial potential. (The error bar represents the standard deviation of three independent electrodes.)

Li_2S_8 solution was added dropwise on ReS_2/CC and Fe−ReS_2/CC and assembled into a button battery for testing.

2.3. Lithium Polysulfide Adsorption Tests. Sulfur powder and lithium sulfide (Li_2S) were mixed in a certain molar ratio. Then, a certain amount of DME/DOL solution (v/v = 1/1) was added. It was stirred continuously overnight in an argon glovebox to synthesize the required Li_2S_6 solution. CC, ReS_2, and Fe−ReS_2 were cut into round slices with a diameter of 12 mm. They were immersed in a 2 mL Li_2S_6 solution and observed for a color change after 6 h.

2.4. Assembly of Li_2S_6 Symmetric Cells. The prepared sample was cut into a round electrode with a diameter of 12 mm. In the symmetrical battery test, two identical electrodes were used as the working electrode and the opposite electrode to assemble a button-type battery in the glovebox. 20 μL of the Li_2S_6 solution was added to the symmetric cells. The specific scanning speed parameters were set as 1 and 10 mV s^{-1} and the voltage parameter range as −1 to 1 V, and then the battery on the electrochemical workstation was tested (Chenhua Instruments Co., Ltd. China).

2.5. Nucleation and Dissolution Experiment of Li_2S. For the Li_2S precipitation test, CR2032 cells were assembled with the above electrodes (CC, ReS_2, and Fe−ReS_2). An electrolyte containing 0.3 M Li_2S_8 and a blank electrolyte were prepared, and a certain amount of it was added dropwise on the cathode and anode electrodes, respectively. The batteries were discharged to 2.06 V at 0.112 mA through a LAND battery test station. Li_2S was nucleated by discharging at 2.05 V. For the measurement of Li_2S dissolution, in contrast to the nucleation process, only the potential parameters were changed.

2.6. Assembly and Measurement of the Li−S Battery. In the glovebox, a certain amount of the electrolyte was added to assemble a coin-type battery with lithium as the anode and Fe−ReS_2 as the cathode (the active material comes from the prepared Li_2S_8 solution). Each 13 μL of electrolyte contained 1 mg of sulfur. The LAND battery test station was used to perform the galvanostatic cycling tests between 1.7 and 2.8 V. On CHI 660E (Chenhua Instruments Co., Ltd. China), cyclic voltammetry (CV) was performed at different scan rates in the voltage range of 1.7−2.8 V. The test frequency range of electrochemical impedance spectroscopy (EIS) was 100 kHz to 10 mHz.

2.7. Sample Characterization. The micromorphology and size of cathode samples were investigated by scanning electron microscopy (SEM) (SU8020, Japan). The further fine structural characteristics of the surface and interior of the material with the nanometer scale and the crystal plane of the as-synthesized were characterized by transmission electron microscopy (TEM) (Tecnai G2 F30, FEI). X-ray photoelectron spectroscopy (XPS) was performed using Thermo ESCALAB 250xi. In the scanning range of 5 to 85°, the crystal structure of the final product was tested by X-ray diffraction (XRD, Bruker D8 ADVANCE diffractometer) with Cu K radiation (=1.5418 Å). Raman spectra of the samples were obtained using a spectrometer (Jobin-Yvon LabRAM HR EVOLUTION micro-Raman) with a 532 nm laser wavelength. The thickness of Fe−ReS_2 nanosheets was measured using a commercial atomic force microscopy (AFM) system (Dimension Icon, Bruker).

2.8. Computational Methods. The DFT calculations were carried out using the Vienna ab initio simulation package[44,45] by the frozen-core all-electron projector-augment-wave[46,47] method. The Perdew−Burke−Ernzerhof[48] of generalized gradient approximation was adopted to describe the exchange and correlation potential. The cutoff energy for the plane-wave basis set was set to 450 eV. A monolayer 2 × 3 ReS_2(002) slab was used, and a vacuum region of 15 Å above it was used to ensure decoupling between neighboring systems. The Fe-doped ReS_2(002) model was built by replacing two Re atoms of a pure ReS_2(002) slab with two Fe atoms. Geometry optimizations were performed until the forces on each ion were reduced below 0.02 eV/Å. The Monkhorst−Pack *k*-point[49] sampling was set to 3 × 3 × 1. The van der Waals (vdW) interactions were considered by using the DFT-D2 method of Grimme.[50]

The Gibbs free energy (ΔG) was calculated as

https://doi.org/10.1021/acsami.2c14282
ACS Appl. Mater. Interfaces 2022, 14, 50870−50879

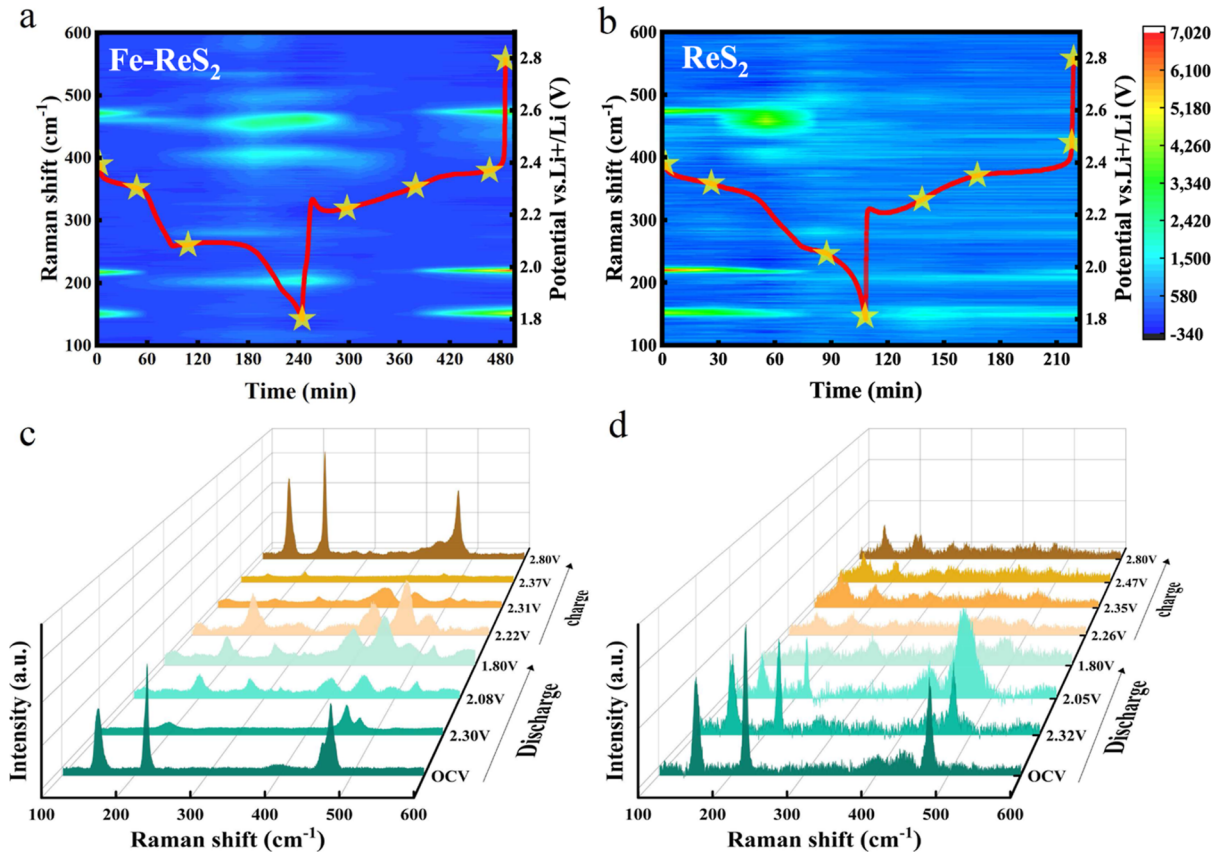

Figure 3. In situ Raman measurement of the ReS_2/CC/S and Fe−ReS_2/CC/S electrodes during charge and discharge. (a,b) In situ time-resolved Raman images of Fe−ReS_2/CC/S and ReS_2/CC/S, respectively. (c,d) The 3D images are the selective Raman spectra of Fe−ReS_2/CC/S and ReS_2/CC/S. The red curves inserted in (a,b) are the voltage−time curves corresponding to the Fe−ReS_2/CC/S and ReS_2/CC/S respectively.

$$\Delta G = \Delta E_{ads} + \Delta E_{ZPE} - T\Delta S$$

The adsorption energy (ΔE_{ads}) was calculated using the expression $\Delta E_{ads} = E_{molecule+surface} - E_{surface} - E_{molecule}$, where $E_{surface}$ is the energy of the clean or Fe−ReS_2(002) surfaces, $E_{molecule}$ represents the energy of the Li_2S, Li_2S_2, Li_2S_4, Li_2S_6, Li_2S_8, or S_8, and $E_{molecule+surface}$ represents the total energy of the adsorbed system.[51] ΔE_{ZPE} is the difference value corresponding to the zero-point energy between the adsorbed molecule and the gas-phase molecule. ΔS is a molecule entropy between the absorbed state and the gas phase.

3. RESULTS AND DISCUSSION

In situ growth of ultrathin Fe−ReS_2 nanosheets on CC by a simple hydrothermal method is shown in Figure 1a.[52] More synthesis details can be found in the Experimental Section of the Supporting Information. The SEM image (Figure 1b) showed that the dense Fe−ReS_2 nanosheets were uniformly coated on the CC. The microstructure of Fe−ReS_2 was characterized by TEM. The 2D layered nanostructure of Fe−ReS_2 can be observed in Figure 1c. The high-resolution TEM (HRTEM) image in Figure S1 shows significant lattice fringe spacings of 0.262 and 0.278 nm. They roughly correspond to the Fe−ReS_2(200) and (020) planes in the XRD diagram. As the doping in the XRD image only has a little red shift, it further indicates that the doping process is based on ReS_2.[53−55] Moreover, Figure 1d shows a lattice plane with an interlayer spacing of 0.629 nm, corresponding to the (002) plane of double-layered Fe−ReS_2. The elemental mapping image (Figure 1e) confirms the relatively uniform distribution of Re, S, and Fe elements in typical Fe−ReS_2 nanostructures. It mainly shows that iron is successfully introduced into ReS_2.[52,64] AFM linear scan (Figure 1f) reveals that the thickness of Fe−ReS_2 nanosheet is 1.06 nm, which is superior to other synthesis strategies.[29,30,43,52] It can be seen that compared with the nanosheets prepared by doping 0.238 mmol ferric chlorides, the nanosheets prepared by the other four concentrations have obvious structural shortcomings, such as Figure S13a−c small volume, Figure S13d small quantity, and size, so they cannot effectively improve the battery performance. It can be seen in Figure S19 that the performance of iron doping with four different concentrations is not ideal. XRD was carried out to identify the phase structure and components of the as-prepared samples. As shown in Figure 1g, the peaks at 14.6, 32.2, and 36.2° corresponded to (002), (020), and ($2\bar{1}2$) planes of ReS_2 (JCPDS 89-0341), respectively. After the Fe doping, the peak of the (001) plane shifts to a higher angle, which might be attributed to the introduction of a smaller atom.

The XPS spectra were utilized to further elucidate the chemical composition and valence state. As shown in Figure S2c,d, two peaks of Re located at 42.2 and 44.7 eV can be attributed to $4f^{7/2}$ and $4f^{5/2}$ of Fe−ReS_2. The high-resolution S 2p (Figure S2e,f) spectrum exhibits two peaks at 162.8 and 164.1 eV ascribed to S $2p^{3/2}$ and S $2p^{1/2}$ of Re−S bonds, respectively. Figure S2b shows the Fe 2p spectrum of Fe−ReS_2, in which two peaks at 708.5 and 721 eV are attributed to Fe $2p^{3/2}$ and $2p^{1/2}$, respectively, indicating that the Fe element is successfully incorporated into ReS_2.[52]

To gain insight into the catalytic ability of electrocatalysts for LiPS redox, the symmetric cells with Li_2S_6 electrolytes were studied by CV.[57,58] The CV curve of Fe−ReS_2 (Figure 2a)

https://doi.org/10.1021/acsami.2c14282
ACS Appl. Mater. Interfaces 2022, 14, 50870−50879

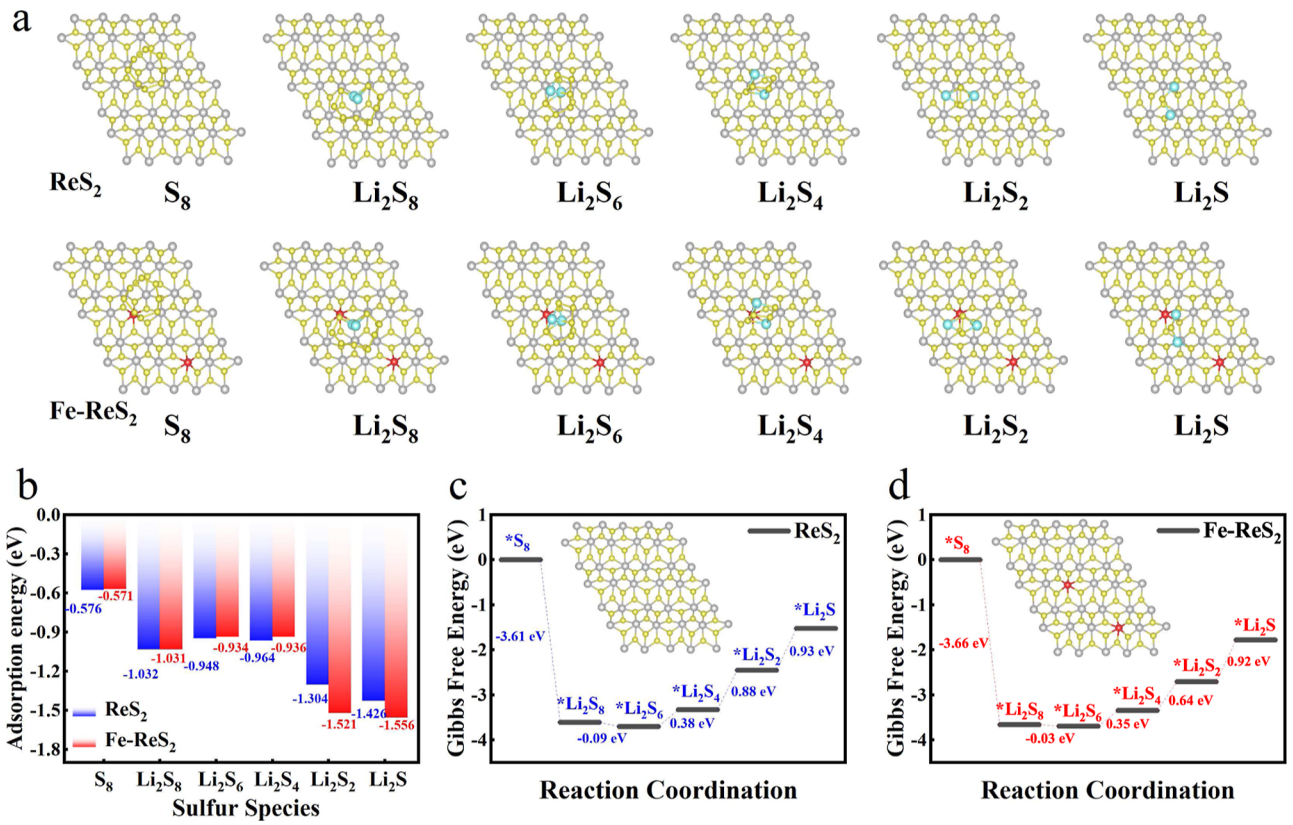

Figure 4. (a) Adsorption optimization conformation of intermediate species on ReS_2 and Fe−ReS_2. (b) Comparison of adsorption energies between the Li_2S_n and Fe−ReS_2 monolayer or ReS_2 monolayer. Energy profiles for the reaction of Li_2S_n on (c) ReS_2 and (d) Fe−ReS_2.

shows higher current density than ReS_2 and CC, indicating the rapid LiPS conversion kinetics. Moreover, the Fe−ReS_2 (Figure 2a) shows narrower redox peaks and smaller peak separation compared with other electrodes (CC and ReS_2). This further proves that Fe−ReS_2 promotes the redox reaction of LiPSs. The CV characteristics of Li−S batteries were also measured to reveal the multiple redox reactions and reversible nature during the charge/discharge process. As shown in Figure 2b, the two representative reduction peaks and one oxidation peak in CV curves are attributed to the reaction of $S_8^{2-} \rightarrow S_4^{2-}$, $S_4^{2-} \rightarrow Li_2S_2/Li_2S$, and $Li_2S_2/Li_2S \rightarrow S_8$, respectively. It is encouraging that the oxidation peak of Fe−ReS_2/S moves to the negative potential, while the two reduction peaks shift to the positive potential (Figure S3). This shows that the kinetics of LiPSs in liquid−solid conversion is promoted. In addition, a Tafel diagram of the reduction process was generated to quantify the catalytic activity. As shown in Figure S22c,d, the Tafel slopes of Fe−ReS_2 are 190.03 and 288.14 mV dec^{-1}, lower than those of ReS_2 (261.66 and 443.27 mV dec^{-1}). It can be seen that the doping of iron improves the catalytic activity of the material. The CV curves (Figure 2b) show almost an identical curve track during the latter cycles, demonstrating the electrochemical stability.

For lithium−sulfur batteries, their specific capacity and sulfur utilization are usually determined by the nucleation behavior of Li_2S during discharge. To study Li_2S nucleation kinetics, the electrochemical deposition of LiPSs from the liquid phase to the solid phase was studied by potentiostatic nucleation measurement. As shown in Figure 2c,d, the peak current of Fe−ReS_2 in the Li_2S deposition occurs earlier than that of ReS_2. This phenomenon indicates that solid Li_2S nucleates rapidly under the catalysis of Fe−ReS_2.[59] The nucleation capacity of Li_2S was calculated according to Faraday's law. The Fe−ReS_2 electrode exhibits a considerably greater Li_2S precipitation capacity (560.49 mA h g_S^{-1}) than that of ReS_2 (479.99 mA h g_S^{-1}) and CC (Figure S4a, 413.05 mA h g_S^{-1}), demonstrating that the Fe−ReS_2 ultrathin nanosheets effectively promote the fast conversion of Li_2S.[60] Due to the accelerated oxidation and dissolution by Fe−ReS_2, the Li_2S dissolution process shows higher dissolution capacity, higher dissolution current density, and a faster dissolution rate than other electrocatalysts (Figure S4b,d).

The sulfur reduction reaction kinetics are mainly determined by the charge transfer ability of the electrocatalyst−adsorbate interface. Consequently, in order to study the origin of the enhanced electrocatalytic activity and kinetics, the electrochemical impedance was measured. Compared with other electrocatalysts, Fe−ReS_2 shows a smaller charge transfer resistance (Figure 2e), suggesting superior charge transfer kinetics during the sulfur reduction reaction.[61] The EIS tests can be used to fit the charge transfer resistance in the sulfur reduction reaction at different temperatures. Therefore, the activation energy of the corresponding reaction is enabled and calculated by the Arrhenius equation (Figure S9). As shown in Figure 2f, the activation energy of Fe−ReS_2 is obviously lower than that of other catalysts (CC and ReS_2), revealing the superior sulfur reduction reaction (SRR) catalytic activity.[62]

Long- and medium-chain LiPSs can be quantitatively evaluated and easily identified through Raman spectroscopy. Therefore, the detailed evolution of LiPS species during charging and discharging was monitored by in situ Raman measurement. The Raman laser is focused on the nanosheets of the electrocatalyst, and the device diagram of the in situ Raman

https://doi.org/10.1021/acsami.2c14282
ACS Appl. Mater. Interfaces 2022, 14, 50870−50879

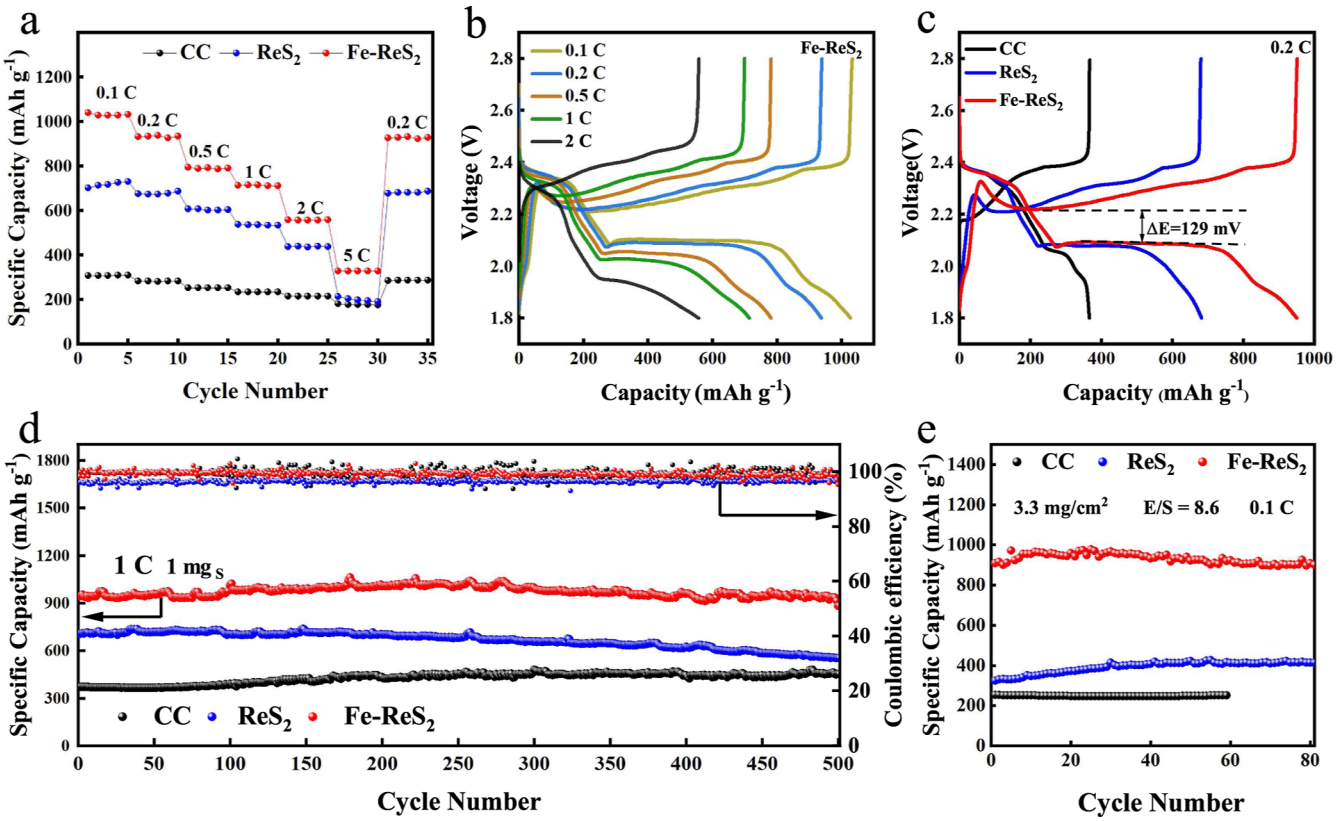

Figure 5. (a) Rate performances of the CC, ReS_2, and Fe−ReS_2. (b) Voltage curve of a standard battery with a lithium foil anode and Fe−ReS_2 cathode at a rate of 0.1 to 2 C. (c) Voltage profiles of CC, ReS_2, and Fe−ReS_2 at C/5 rate. (d) Long-term cycling performance of Li−S cells with CC, ReS_2, and Fe−ReS_2 cathodes at 1 C rate for 500 cycles. (e) Cycle performance of CC, ReS_2, and Fe−ReS_2 with a sulfur load of 3.3 mg cm^{-2} in the voltage range of 1.8−2.8 V and the current rate of 0.1 C.

laser is shown in Figure S5. As shown in time-resolved Raman spectroscopy images (Figure 3a,b), various LiPSs can be distinguished during discharge processes. Three characteristic peaks with powerful intensities at 150, 219, and 474 cm^{-1} (Figure 3c) are clearly detected at the open-circuit voltage, which is attributed to the antisymmetric bond bending, symmetric bond bending, and symmetric bond stretching modes of S_8^{2-}, indicating that a large quantity of Li_2S_8 has been adsorbed on the surface of catalysts. When the cell is discharged to 2.08 V, the intensities of peaks at 202 and 398 cm^{-1} become stronger. This is due to the conversion of Li_2S_8 to Li_2S_6 and Li_2S_4.[S6] By comparing Figure 3a,b, it is obvious that Fe−ReS_2 accurately appears at the peak of short-chain Li_2S_2 with high intensity in the late stage of discharge, while ReS_2 does not appear. Therefore, Fe−ReS_2 reduces the energy barrier from Li_2S_4 to Li_2S_2, allowing the appearance of Li_2S_2 in the late discharge period to be observed in the Raman image. Then, the conversion barrier will also be reduced for the solid−solid conversion process. It is also found that the energy barrier of Li_2S_4 to Li_2S_2 decreases significantly in the theoretical calculation, which shows that Fe−ReS_2 is more conducive to a sulfur reduction in the thermodynamic aspect. Fe−ReS_2 has a stronger catalytic effect on the polysulfide transformation during discharge. During charging, the Li_2S_2 peaks gradually are converted to Li_2S_4 and Li_2S_6 peaks, and these intermediates were completely replaced by Li_2S_8 peaks at a charge voltage of 2.8 V. In contrast, neither the discharge nor the charge process can realize effective LiPS conversion by using ReS_2 as a catalyst, which will lead to capacity loss of Li−S batteries. Corporately, the ultrathin Fe−ReS_2 nanosheets as electrocatalysts can accelerate the sulfur reduction kinetics during the discharge of the lithium−sulfur battery. It can also improve the oxidation kinetics of Li_2S_2 during the charging process of a lithium−sulfur battery.

To attain an in-depth understanding of the enhanced discharge reaction kinetics of the electrocatalytic reaction, the adsorption geometries of LiPSs on the optimized Fe−ReS_2 and ReS_2 models are shown in Figure 4a. At the same time, the contrast of the state density images (Figures S11 and S12) can prove that the Fe doping Fisherome grade movement toward the guide band, the band gap is reduced, and the electrical conductivity of the material itself can be improved. The adsorption energies of unlithiated S_8 and LiPS intermediates on Fe−ReS_2 are higher than that of ReS_2 in Figure 4b. The intrinsic ability of Fe−ReS_2 strengthens chemical interactions with intermediates, which simultaneously prevents the premature desorption of LiPSs and enhances the sulfur reduction reaction kinetics. As shown in Figure S6, the solution with Fe−ReS_2 is entirely decolored, while the control solution with ReS_2 and pure CC exhibit negligible discoloration. The visual adsorption experiment proves that the Fe−ReS_2 possesses superior adsorptivity of LiPSs than other catalysts (CC and ReS_2).

In addition, the Gibbs free energies for all of the reaction steps were calculated for both ReS_2 and Fe−ReS_2 catalysts (Figure 4c,d). The first reduction step of S_8 to Li_2S_8 shows a spontaneous exothermic reaction on all the catalysts. The following four reduction processes with stepwise formation of Li_2S_6, Li_2S_4, Li_2S_2, and Li_2S are endothermic reactions. Notably, Li_2S_2 and Li_2S formation possesses the largest positive Gibbs free energy

https://doi.org/10.1021/acsami.2c14282
ACS Appl. Mater. Interfaces 2022, 14, 50870−50879

compared to other steps, indicating that the formation of final insoluble products is the rate-determining step for Li−S batteries. The lower Gibbs free energies for sulfur reduction demonstrate the thermodynamically favorable of the Fe−ReS_2 catalyst compared with bare ReS_2, which matches well with the aforementioned results of Li_2S nucleation and in situ Raman spectroscopy.

Although the superior electrocatalyst activity of Fe−ReS_2 ultrathin nanosheets is demonstrated by previous experiments and theoretical calculation, it is important to evaluate the feasibility of Fe−ReS_2/S for practical Li−S batteries. As shown in Figure 5a, the Fe−ReS_2/S electrode exhibits an excellent rate performance, delivering highly reversible specific capacities of 1030.5, 932.7, 789.3, 710.5, 557.6, and 327.8 mA h g^{-1} from 0.1 to 5 C, respectively. In comparison, cells with the lower catalytic activity of bare ReS_2 and CC possess unsatisfactory discharge capacities. The galvanostatic intermittent titration technique (GITT) test (Figure S15a,b) shows that Fe−ReS_2 has the longest time to complete the same charge and discharge cycle. Then, the corresponding diffusion coefficient D is calculated roughly. There is a difference of 1 order of magnitude in the diffusion coefficient D of the Fe−ReS_2 electrode during charging and a difference of 2 orders of magnitude in the diffusion coefficient D during discharge. Therefore, we can indirectly prove that this modification can also improve the discharge rate to a certain extent and improve the dynamics process inside the battery. The charge/discharge voltage profiles (Figure 5b) show two charge/discharge plateaus, which can be clearly observed at a high rate of 2 C. Furthermore, the Fe−ReS_2/S exhibits the smallest polarization voltage gap (129 mV) compared with bare ReS_2/S (222 mV) and carbon cloth/S (326 mV) electrodes (Figure 5c), indicating low battery polarization, high voltage efficiency, high reversibility, larger specific capacity, and fast LiPS conversion kinetics.[63−65] As shown in Figure S14a,b, the contribution of the material's own capacitance in the overall capacity is relatively small, so it does not affect the contribution of Fe−ReS_2 in the performance improvement of lithium−sulfur batteries.

The cycling stability of cells with these electrocatalysts was measured at 1 C. As shown in Figure 5d, when utilizing the Fe−ReS_2 as an electrocatalyst, the cell delivers a high initial specific capacity of 942.4 mA h g^{-1} and a stable cycling performance of more than 500 cycles with an extremely low capacity decay of 0.013% per cycle. It can be seen in Figure S16 that in 1000 cycles, the cycle attenuation rate of each cycle can be calculated to be only 0.0337%, which shows the stability of the battery itself. In Figures S17 and S18, the attenuation rate of each cycle of the long cycle at different magnifications is 0.071% (2 C) and 0.035% (5 C), respectively. In contrast, the ReS_2/S and carbon cloth/S show low initial capacity and severe capacity decay. The cycling performance of cells with increased sulfur loading of 3.3 mg cm^{-2} at 0.1 C is further measured. The Fe−ReS_2/S electrode delivers a higher capacity of 900.5 mA h g^{-1} than that of ReS_2/S (413.1 mA h g^{-1}) and CC/S (251 mA h g^{-1}). As shown in Figure S20, the Fe−ReS_2/S electrode also showed good performance when the load was increased, for example, 579 mA h g^{-1} for 5 mg sulfur load and 510.7 and 231.3 mA h g^{-1} for 8 and 10 mg sulfur load, respectively. Such remarkable improvement in Li−S battery performance can be ascribed to the merits of the designed Fe−ReS_2 catalyst including good conductivity, stronger LiPSs adsorption, and efficient catalytic conversion of LiPSs. The electrochemical cycle stability performance of the Fe−ReS_2 electrode is also superior to some of the representative cathode hosts in recent literature, as outlined in Table S1 (Supporting Information). From Table S1, it can be found that compared with carbon membranes such as graphene oxide, carbon nanotubes, and carbon nanofibers, the capacity attenuation ratio of each cycle of this work has obvious advantages. For ReS_2, our work also has a good capacity retention capability. Therefore, it can also provide a good exploration direction for the follow-up research.

4. CONCLUSIONS

In conclusion, we proposed Fe−ReS_2 ultrathin nanosheets which possess high electrical conductivity and abundant active sites to trap LiPSs and improve the sulfur redox kinetics. Benefiting from superior electrocatalytic activity, highly reversible specific capacity and long lifetime for Li−S batteries without LiPS accumulation were achieved. Based on the in situ Raman measurements, electrochemical analysis, and theoretical calculations, the above results were obtained. This work provides a simple strategy for designing a TMD ultrathin nanosheet electrocatalyst, promising for the development of 2D electrocatalysts in Li−S batteries.

■ ASSOCIATED CONTENT

Supporting Information

The Supporting Information is available free of charge at https://pubs.acs.org/doi/10.1021/acsami.2c14282.

HRTEM images of Fe−ReS_2 nanosheets; XPS spectra for Re 4f, S 2p, and Fe 2p regions of ReS_2 and Fe−ReS_2; CV curves about CC, ReS_2, and Fe−ReS_2; potentiostatic discharge curve on CC, potentiostatic charge curves on CC, ReS_2, and Fe−ReS_2; in situ Raman measuring instrument; adsorption tests of lithium polysulfide; flow diagram of making Fe−ReS_2/CC; elemental mapping images of Fe−ReS_2/CC; Arrhenius plot about CC, ReS_2, and Fe−ReS_2; CV curve of Li_2S_6 symmetrical battery with CC, ReS_2, and Fe−ReS_2; density of states of ReS_2 and Fe−ReS_2; SEM images of different Fe content; capacitance contribution of ReS_2 and Fe−ReS_2; GITT voltage profile of ReS_2 and Fe−ReS_2; long-term cycling performance at a 1, 2, and 5 C rate; long-term cycling performance with different iron concentrations; cycle performance with a sulfur load of 5, 8, and 10 mg cm^{-2}; cycling performance comparison of Fe−ReS_2/CC electrode; Fe content with different amount of ferric chloride; LSV curves; and Tafel plots (PDF)

■ AUTHOR INFORMATION

Corresponding Authors

Liyan Shang − *Technical Center for Multifunctional Magneto-Optical Spectroscopy (Shanghai), Engineering Research Center of Nanophotonics & Advanced Instrument (Ministry of Education), Department of Physics, School of Physics and Electronic Science, East China Normal University, Shanghai 200241, China;* orcid.org/0000-0003-2341-3978; Phone: +86-21-54345150; Email: lyshang@ee.ecnu.edu.cn; Fax: +86-21-54342933

Zhigao Hu − *Technical Center for Multifunctional Magneto-Optical Spectroscopy (Shanghai), Engineering Research Center of Nanophotonics & Advanced Instrument (Ministry of Education), Department of Physics, School of Physics and Electronic Science, East China Normal University, Shanghai 200241, China; Collaborative Innovation Center of Extreme*

https://doi.org/10.1021/acsami.2c14282
ACS Appl. Mater. Interfaces 2022, 14, 50870−50879

Optics, Shanxi University, Taiyuan 030006, China; orcid.org/0000-0003-0575-2191; Email: zghu@ee.ecnu.edu.cn

Authors

Jianli Tang − *Technical Center for Multifunctional Magneto-Optical Spectroscopy (Shanghai), Engineering Research Center of Nanophotonics & Advanced Instrument (Ministry of Education), Department of Physics, School of Physics and Electronic Science, East China Normal University, Shanghai 200241, China*

Chunqiao Jin − *Technical Center for Multifunctional Magneto-Optical Spectroscopy (Shanghai), Engineering Research Center of Nanophotonics & Advanced Instrument (Ministry of Education), Department of Physics, School of Physics and Electronic Science, East China Normal University, Shanghai 200241, China*

Liuxiang Huo − *Technical Center for Multifunctional Magneto-Optical Spectroscopy (Shanghai), Engineering Research Center of Nanophotonics & Advanced Instrument (Ministry of Education), Department of Physics, School of Physics and Electronic Science, East China Normal University, Shanghai 200241, China*

Shenyu Du − *Technical Center for Multifunctional Magneto-Optical Spectroscopy (Shanghai), Engineering Research Center of Nanophotonics & Advanced Instrument (Ministry of Education), Department of Physics, School of Physics and Electronic Science, East China Normal University, Shanghai 200241, China*

Xionghu Xu − *Technical Center for Multifunctional Magneto-Optical Spectroscopy (Shanghai), Engineering Research Center of Nanophotonics & Advanced Instrument (Ministry of Education), Department of Physics, School of Physics and Electronic Science, East China Normal University, Shanghai 200241, China*

Yuting Yan − *Technical Center for Multifunctional Magneto-Optical Spectroscopy (Shanghai), Engineering Research Center of Nanophotonics & Advanced Instrument (Ministry of Education), Department of Physics, School of Physics and Electronic Science, East China Normal University, Shanghai 200241, China*

Kai Jiang − *Technical Center for Multifunctional Magneto-Optical Spectroscopy (Shanghai), Engineering Research Center of Nanophotonics & Advanced Instrument (Ministry of Education), Department of Physics, School of Physics and Electronic Science, East China Normal University, Shanghai 200241, China*

Jinzhong Zhang − *Technical Center for Multifunctional Magneto-Optical Spectroscopy (Shanghai), Engineering Research Center of Nanophotonics & Advanced Instrument (Ministry of Education), Department of Physics, School of Physics and Electronic Science, East China Normal University, Shanghai 200241, China;* orcid.org/0000-0003-1511-4281

Yawei Li − *Technical Center for Multifunctional Magneto-Optical Spectroscopy (Shanghai), Engineering Research Center of Nanophotonics & Advanced Instrument (Ministry of Education), Department of Physics, School of Physics and Electronic Science, East China Normal University, Shanghai 200241, China;* orcid.org/0000-0001-8776-5687

Junhao Chu − *Technical Center for Multifunctional Magneto-Optical Spectroscopy (Shanghai), Engineering Research Center of Nanophotonics & Advanced Instrument (Ministry of Education), Department of Physics, School of Physics and Electronic Science, East China Normal University, Shanghai 200241, China; Collaborative Innovation Center of Extreme Optics, Shanxi University, Taiyuan 030006, China*

Complete contact information is available at: https://pubs.acs.org/10.1021/acsami.2c14282

Author Contributions

J.T. and C.J. contributed equally to this work. J.T., C.J., L.S., and Z.H. initiated and designed the experiments and wrote the manuscript. J.T., J.Z., and Y.L. conducted and gave a discussion about the theoretical calculation. J.T., C.J., L.H., S.D., X.X., and Y.Y. carried out the experiment for sample fabrications. K.J., Z.H., and J.C. carried out experimental analyses and the underlying mechanism. All of the authors contributed to the manuscript preparation.

Notes

The authors declare no competing financial interest.

■ ACKNOWLEDGMENTS

This work was financially supported by the National Natural Science Foundation of China (grant no. 62090013), the National Key Research and Development Program of China (grant no. 2019YFB2203403), the National Natural Science Foundation of China (grants nos. 61974043, 62074058, and 91833303), the Projects of Science and Technology Commission of Shanghai Municipality (grants nos. 21JC1402100 and 19511120100), and the Program for Professor of Special Appointment (Eastern Scholar) at Shanghai Institutions of Higher Learning and Shanghai Pujiang Program (20PJ1403600).

■ REFERENCES

(1) Service, R. F. Lithium-sulfur batteries poised for leap. *Science* **2018**, *359*, 1080−1081.

(2) Pang, Q.; Liang, X.; Kwok, C. Y.; Nazar, L. F. Advances in lithium-sulfur batteries based on multifunctional cathodes and electrolytes. *Nat. Energy* **2016**, *1*, 16132.

(3) Chang, J.; Shang, J.; Sun, Y.; Ono, L. K.; Wang, D.; Ma, Z.; Huang, Q.; Chen, D.; Liu, G.; Cui, Y. Flexible and stable high-energy lithium-sulfur full batteries with only 100% oversized lithium. *Nat. Commun.* **2018**, *9*, 4480.

(4) Zhang, H.; Ono, L.; Tong, G. Q.; Liu, Y. Q.; Qi, Y. B. Long-life lithium-sulfur batteries with high areal capacity based on coaxial CNTs@TiN-TiO_2 sponge. *Nat. Commun.* **2021**, *12*, 4738.

(5) Li, H. H.; Chen, H. Q.; Xue, Y.; Zhang, Y. T.; Zhang, M. J.; Yu, W. Q.; Bai, G. Y.; Zhuo, K. L.; Zheng, Y. P. Catalytic and Dual-Conductive Matrix Regulating the Kinetic Behaviors of Polysulfides in Flexible Li-S Batteries. *ACS Appl. Mater. Interfaces* **2020**, *10*, 2001683.

(6) Yan, B.; Li, X. F.; Xiao, W.; Hu, J. H.; Zhang, L. L.; Yang, X. L. Design, synthesis, and application of metal sulfides for Li-S batteries: progress and prospects. *J. Mater. Chem. A* **2020**, *8*, 17848−17882.

(7) Hu, A.; Chen, W.; Du, X. C.; Hu, Y.; Lei, T. Y.; Wang, H. B.; Xue, L. X.; Li, Y. Y.; Sun, H.; Yan, Y. C.; Long, J. P.; Shu, C. Z.; Zhu, J.; Li, B. H.; Wang, X. F.; Xiong, J. An artificial hybrid interphase for an ultrahigh-rate and practical lithium metal anode. *Energy Environ. Sci.* **2021**, *14*, 4115.

(8) He, J.; Chen, Y. F.; Li, P. J.; Fu, F.; Wang, Z. G.; Zhang, W. L. Three-dimensional CNT/graphene-sulfur hybrid sponges with high sulfur loading as superior-capacity cathodes for lithium-sulfur batteries. *J. Mater. Chem. A* **2015**, *3*, 18605.

(9) Wang, H.-E.; Yin, K. L.; Zhao, X.; Qin, N.; Li, Y.; Deng, Z.; Zheng, L. C.; Su, B.-L.; Lu, Z. G. Coherent TiO_2/$BaTiO_3$ heterostructure as a functional reservoir and promoter for polysulfide intermediates. *Chem. Commun.* **2018**, *54*, 12250−12253.

(10) Wang, H.-E.; Yin, K. L.; Qin, N.; Zhao, X.; Xia, F.-J.; Hu, Z.-Y.; Guo, G. L.; Cao, G. Z.; Zhang, W. J. Oxygen-deficient titanium dioxide as a functional host for lithium-sulfur batteries. *J. Mater. Chem. A* **2019**, *7*, 10346−10353.
(11) Song, J.-P.; Wu, L.; Dong, W.-D.; Li, C.-F.; Chen, L.-H.; Dai, X.; Li, C.; Chen, H.; Zou, W.; Yu, W.-B.; Hu, Z.-Y.; Liu, J.; Wang, H.-E.; Li, Y.; Su, B.-L. MOF-derived nitrogen-doped core-shell hierarchical porous carbon confining selenium for advanced lithium-selenium batteries. *Nanoscale* **2019**, *11*, 6970−6981.
(12) Li, X. C.; Guo, G. L.; Qin, N.; Deng, Z.; Lu, Z. G.; Shen, D.; Zhao, X.; Li, Y.; Su, B.-L.; Wang, H.-E. SnS_2/TiO_2 nanohybrids chemically bonded on nitrogen-doped graphene for lithium-sulfur batteries: synergy of vacancy defects and heterostructures. *Nanoscale* **2018**, *10*, 15505−15512.
(13) Meng, L. S.; Yao, Y.; Liu, J.; Wang, Z.; Qian, D.; Zheng, L. C.; Su, B.-L.; Wang, H.-E. $MoSe_2$ nanosheets as a functional host for lithium-sulfur batteries. *J. Energy Chem.* **2020**, *47*, 241−247.
(14) Chen, H.; Dong, W.-D.; Xia, F.-J.; Zhang, Y.-J.; Yan, M.; Song, J.-P.; Zou, W.; Liu, Y.; Hu, Z.-Y.; Liu, J.; Li, Y.; Wang, H.-E.; Chen, L.-H.; Su, B.-L. Hollow nitrogen-doped carbon/sulfur@MnO_2 nanocomposite with structural and chemical dual-encapsulation for lithium-sulfur battery. *Chem. Eng. J.* **2020**, *381*, 122746.
(15) Hu, A.; Zhou, M. J.; Lei, T. Y.; Hu, Y.; Du, X. C.; Gong, C. H.; Shu, C. Z.; Long, J. P.; Zhu, J.; Chen, W.; Wang, X. F.; Xiong, J. Optimizing Redox Reactions in Aprotic Lithium-Sulfur Batteries. *Adv. Energy Mater.* **2020**, *10*, 2002180.
(16) Zhou, X.; Liu, T. T.; Zhao, G. F.; Yang, X. F.; Guo, H. Cooperative catalytic interface accelerates redox kinetics of sulfur species for high-performance Li-S batteries. *Energy Storage Mater.* **2021**, *40*, 139−149.
(17) Shi, Z. X.; Li, M.; Sun, J. Y.; Chen, Z. W. Defect Engineering for Expediting Li-S Chemistry: Strategies, Mechanisms, and Perspectives. *Adv. Energy Mater.* **2021**, *11*, 2100332.
(18) Liu, F.; Sun, G.; Wu, H. B.; Chen, G.; Lu, Y. Dual redox mediators accelerate the electrochemical kinetics of lithium-sulfur batteries. *Nat. Commun.* **2020**, *11*, 5215.
(19) Peng, L. L.; Wei, Z. Y.; Wan, C. Z.; Chen, Z.; Zhu, D.; Baumann, D.; Liu, H. T.; Allen, C. S.; Xu, X.; Kirkland, A. I.; Shakir, I.; Almutairi, Z.; Tolbert, S.; Dunn, B.; Huang, Y.; Sautet, P.; Duan, X. F. A fundamental look at electrocatalytic sulfur reduction reaction. *Nat. Catal.* **2020**, *3*, 762−770.
(20) Wang, Y.; Zhou, L. P.; Huang, J. Y.; Wang, X. Y.; Xu, X. L.; Lu, J. G.; Tian, Y.; Ye, Z. Z.; Tang, H. C.; Lee, S.-T.; Lu, Y. Y. Highly Stable Lithium-Sulfur Batteries Promised by Siloxene: An Effective Cathode Material to Regulate the Adsorption and Conversion of Polysulfides. *Adv. Funct. Mater.* **2020**, *30*, 1910331.
(21) Lei, T.; Chen, W.; Huang, J.; Yan, C.; Sun, H.; Wang, C.; Zhang, W.; Li, Y.; Xiong, J. Multi-Functional Layered WS_2 Nanosheets for Enhancing the Performance of Lithium-Sulfur Batteries. *Adv. Energy Mater.* **2017**, *7*, 1601843.
(22) Park, J. J.; Yu, B.-C.; Park, J. S.; Choi, J. W.; Kim, C. J.; Sung, Y.-E.; Goodenough, J. B. Tungsten Disulfide Catalysts Supported on a Carbon Cloth Interlayer for High Performance Li-S Battery. *Adv. Energy Mater.* **2017**, *7*, 1602567.
(23) Yu, B.; Huang, A. J.; Srinivas, K.; Zhang, X. J.; Ma, F.; Wang, X. Q.; Chen, D. J.; Wang, B.; Zhang, W. L.; Wang, Z. G.; He, J. R.; Chen, Y. F. Outstanding Catalytic Effects of 1T-$MoTe_2$ Quantum Dots@3D Graphene in Shuttle-Free Li-S Batteries. *ACS Nano* **2021**, *15*, 13279−13288.
(24) Liu, Y.; Han, M.; Xiong, Q.; Zhang, S.; Zhao, C.; Gong, W.; Wang, G.; Zhang, H.; Zhao, H. Dramatically Enhanced Ambient Ammonia Electrosynthesis Performance by In-Operando Created Li-S Interactions on MoS_2 Electrocatalyst. *Adv. Energy Mater.* **2019**, *9*, 1803935.
(25) Du, S. Y.; Wu, C.; Ao, L. Y.; Zhou, X.; Jiang, K.; Shang, L. Y.; Li, Y. W.; Zhang, J. Z.; Hu, Z. G.; Chu, J. H. Significantly enhanced lithium storage by in situ grown CoS_2@MoS_2 core-shell nanorods anchored on carbon cloth. *Chem. Eng. J.* **2021**, *420*, 127714.
(26) He, J. R.; Hartmann, G.; Lee, M.; Hwang, G. S.; Chen, Y. F.; Manthiram, A. Freestanding 1T MoS_2/graphene heterostructures as a highly efficient electrocatalyst for lithium polysulfides in Li-S batteries. *Adv. Energy Mater.* **2019**, *12*, 344−350.
(27) Yu, B.; Chen, Y. F.; Wang, Z. G.; Chen, D. J.; Wang, X. Q.; Zhang, W. L.; He, J. R.; He, W. D. 1T-MoS_2 nanotubes wrapped with N-doped graphene as highly-efficient absorbent and electrocatalyst for Li-S batteries. *J. Power Sources* **2020**, *447*, 227364.
(28) Cheng, Z. B.; Chen, Y. L.; Yang, Y. S.; Zhang, L. J.; Pan, H.; Fan, X.; Xiang, S. C.; Zhang, Z. J. Metallic MoS_2 Nanoflowers Decorated Graphene Nanosheet Catalytically Boosts the Volumetric Capacity and Cycle Life of Lithium-Sulfur Batteries. *Adv. Energy Mater.* **2021**, *11*, 2003718.
(29) Mukherjee, S.; Banwait, A.; Grixti, S.; Koratkar, N.; Singh, C. V. Adsorption and Diffusion of Lithium and Sodium on Defective Rhenium Disulfide: A First Principles Study. *ACS Appl. Mater. Interfaces* **2018**, *10*, 5373−5384.
(30) Gao, J.; Li, L.; Tan, J. W.; Sun, H.; Li, B. C.; Idrobo, J. C.; Singh, C. V.; Lu, T.-M.; Koratkar, N. Vertically Oriented Arrays of ReS_2 Nanosheets for Electrochemical Energy Storage and Electrocatalysis. *Nano Lett.* **2016**, *16*, 3780−3787.
(31) Liu, B. X.; Chen, B.; Qin, H. Y.; Wang, N.; Liu, E. Z.; Shi, C. S.; Zhao, N. Q. ReS_2 nanosheets anchored on rGO as an efficient polysulfides immobilizer and electrocatalyst for Li-S batteries. *Appl. Surf. Sci.* **2020**, *505*, 144586.
(32) Yuan, H.; Peng, H.-J.; Li, B.-Q.; Xie, J.; Kong, L.; Zhao, M.; Chen, X.; Huang, J.-Q.; Zhang, Q. Conductive and Catalytic Triple-Phase Interfaces Enabling Uniform Nucleation in High-Rate Lithium-Sulfur Batteries. *Adv. Energy Mater.* **2019**, *9*, 1802768.
(33) Zuo, J. H.; Gong, Y. J. Applications of transition-metal sulfides in the cathodes of lithium-sulfur batteries. *Tungsten* **2020**, *2*, 134−146.
(34) Wang, M.; Fan, L. S.; Tian, D.; Wu, X.; Qiu, Y.; Zhao, C. Y.; Guan, B.; Wang, Y.; Zhang, N. Q.; Sun, K. N. Rational Design of Hierarchical SnO_2/1T-MoS_2 Nanoarray Electrode for Ultralong-Life Li-S Batteries. *ACS Energy Lett.* **2018**, *3*, 1627.
(35) Zhu, Z.; Gao, F.; Zhang, Z.; Zhuang, Q.; Fu, M. In-situ growth of $MnCo_2O_4$ hollow spheres on nickel foam as pseudocapacitive electrodes for supercapacitors. *J. Colloid Interface Sci.* **2021**, *587*, 56−63.
(36) Zhu, Z. T.; Zhang, Z. H.; Zhuang, Q. R.; Gao, F.; Liu, Q. Y.; Zhu, X. X.; Fu, M. Growth of $MnCo_2O_4$ hollow nano-spheres on activated carbon cloth for flexible asymmetric supercapacitors. *J. Power Sources* **2021**, *492*, 229669.
(37) Aslan, O. B.; Chenet, D. A.; van der Zande, A. M.; Hone, J. C.; Heinz, T. F. Linearly Polarized Excitons in Single- and Few-Layer ReS_2 Crystals. *ACS Photonics* **2016**, *3*, 96−101.
(38) Rahman, M. Z.; Davey, K.; Qiao, S.-Z. Advent of 2D Rhenium Disulfide (ReS_2): Fundamentals to Applications. *Adv. Funct. Mater.* **2017**, *27*, 1606129.
(39) Liu, S.; Liu, Y.; Lei, W. W.; Zhou, X.; Xu, K.; Qiao, Q. Q.; Zhang, W.-H. Few-layered ReS_2 nanosheets vertically aligned on reduced graphene oxide for superior lithium and sodium storage. *J. Mater. Chem. A* **2018**, *6*, 20267−20276.
(40) Cai, Z.; Zhou, D.; Wang, M.; Bak, S.-M.; Wu, Y.; Wu, Z.; Tian, Y.; Xiong, X.; Li, Y.; Liu, W.; Siahrostami, S.; Kuang, Y.; Yang, X.-Q.; Duan, H.; Feng, Z.; Wang, H.; Sun, X. Introducing Fe^{2+} into Nickel-Iron Layered Double Hydroxide: Local Structure Modulated Water Oxidation Activity. *Angew. Chem., Int. Ed.* **2018**, *57*, 9392.
(41) Wang, X. G.; Meng, L. J.; Li, B. X.; Gong, Y. J. Heteroatoms/molecules to tune the properties of 2D materials. *Mater. Today* **2021**, *47*, 108−130.
(42) Wang, Y.; Deng, Z.; Huang, J. Y.; Li, H. J.; Li, Z. Y.; Peng, X. S.; Tian, Y.; Lu, J. G.; Tang, H. C.; Chen, L. X.; Ye, Z. Z. 2D Zr-Fc metal-organic frameworks with highly efficient anchoring and catalytic conversion ability towards polysulfides for advanced Li-S battery. *Energy Storage Mater.* **2021**, *36*, 466−477.
(43) Fan, S.; Huang, S. Z.; Pam, M. E.; Chen, S.; Wu, Q. Y.; Hu, J. P.; Wang, Y.; Ang, L. K.; Yan, C. C.; Shi, Y. M.; Yang, H. Y. Design Multifunctional Catalytic Interface: Toward Regulation of Polysulfide and Li_2S Redox Conversion in Li-S Batteries. *Small* **2019**, *15*, 1906132.

https://doi.org/10.1021/acsami.2c14282
ACS Appl. Mater. Interfaces 2022, 14, 50870−50879

(44) Kresse, G.; Hafner, J. Ab initio molecular-dynamics simulation of the liquid-metal-amorphous-semiconductor transition in germanium. *Phys. Rev. B: Condens. Matter Mater. Phys.* **1994**, *49*, 14251−14269.
(45) Kresse, G. G.; Furthmüller, J. Efficient Iterative Schemes for Ab Initio Total-Energy Calculations Using a Plane-Wave Basis Set. *Phys. Rev. B: Condens. Matter Mater. Phys.* **1996**, *54*, 11169.
(46) Blöchl, P. E. Projector augmented-wave method. *Phys. Rev. B: Condens. Matter Mater. Phys.* **1994**, *50*, 17953−17979.
(47) Kresse, G.; Joubert, D. From ultrasoft pseudopotentials to the projector augmented-wave method. *Phys. Rev. B: Condens. Matter Mater. Phys.* **1999**, *59*, 1758−1775.
(48) Hammer, B.; Hansen, L. B.; Nørskov, J. K. Improved adsorption energetics within density-functional theory using revised Perdew-Burke-Ernzerhof functionals. *Phys. Rev. B: Condens. Matter Mater. Phys.* **1999**, *59*, 7413−7421.
(49) Monkhorst, H. J.; Pack, J. D. Special points for Brillouin-zone integrations. *Phys. Rev. B: Solid State* **1976**, *13*, 5188−5192.
(50) Grimme, S. Semiempirical GGA-type density functional constructed with a long-range dispersion correction. *J. Comput. Chem.* **2006**, *27*, 1787−1799.
(51) Zhou, C. Y.; Li, X. C.; Jiang, H. L.; Ding, Y.; He, G. H.; Guo, J.; Chu, Z.; Yu, G. H. Pulverizing Fe_2O_3 Nanoparticles for Developing Fe_3C/N-Codoped Carbon Nanoboxes with Multiple Polysulfide Anchoring and Converting Activity in Li-S Batteries. *Adv. Funct. Mater.* **2021**, *31*, 2011249.
(52) Lai, F. L.; Chen, N.; Ye, X. B.; He, G. J.; Zong, W.; Holt, K. B.; Pan, B. C.; Parkin, I. P.; Liu, T. X.; Chen, R. J. Refining Energy Levels in ReS_2 Nanosheets by Low-Valent Transition-Metal Doping for Dual-Boosted Electrochemical Ammonia/Hydrogen Production. *Adv. Funct. Mater.* **2020**, *30*, 1907376.
(53) Zhou, Y.; Song, E.; Zhou, J. D.; Lin, J. H.; Ma, R. G.; Wang, Y. W.; Qiu, W. J.; Shen, R. X.; Suenaga, K.; Liu, Q.; Wang, J. C.; Liu, Z.; Liu, J. J. Auto-optimizing Hydrogen Evolution Catalytic Activity of ReS_2 through Intrinsic Charge Engineering. *ACS Nano* **2018**, *12*, 4486−4493.
(54) Rahman, M.; Davey, K.; Qiao, S. Z. Advent of 2D Rhenium Disulfide (ReS_2): Fundamentals to Applications. *Adv. Funct. Mater.* **2017**, *27*, 1606129.
(55) He, J. R.; Bhargav, A.; Yaghoobnejad Asl, H.; Chen, Y. F.; Manthiram, A. 1T-ReS_2 Nanosheets In Situ Grown on Carbon Nanotubes as a Highly Efficient Polysulfide Electrocatalyst for Stable Li-S Batteries. *Adv. Energy Mater.* **2020**, *10*, 2001017.
(56) Zha, C. Y.; Wu, D. H.; Zhao, Y. W.; Deng, J.; Wu, J. H.; Wu, R.; Yang, M.; Wang, L.; Chen, H. Y. Two-dimensional multimetallic sulfide nanosheets with multi-active sites to enhance polysulfide redox reactions in liquid Li_2S_6-based lithium-polysulfide batteries. *J. Energy Chem.* **2021**, *52*, 163−169.
(57) Li, H. J.; Song, Y. H.; Xi, K.; Wang, W.; Liu, S.; Li, G. R.; Gao, X. P. Sulfur vacancies in Co_9S_{8-x}/N-doped graphene enhancing the electrochemical kinetics for high-performance lithium-sulfur batteries. *J. Mater. Chem. A* **2021**, *9*, 10704−10713.
(58) Li, W.; Chen, K.; Xu, Q.; Li, X.; Zhang, Q.; Weng, J.; Xu, J. Mo_2C/C Hierarchical Double-Shelled Hollow Spheres as Sulfur Host for Advanced Li-S Batteries. *Angew. Chem., Int. Ed.* **2021**, *60*, 21512.
(59) Ye, Z. Q.; Jiang, Y.; Li, L.; Wu, F.; Chen, R. J. Self-Assembly of 0D-2D Heterostructure Electrocatalyst from MOF and MXene for Boosted Lithium Polysulfide Conversion Reaction. *Adv. Mater.* **2021**, *33*, 2101204.
(60) Zhang, G.; Peng, H.-J.; Zhao, C.-Z.; Chen, X.; Zhao, L.-D.; Li, P.; Huang, J.-Q.; Zhang, Q. The Radical Pathway Based on a Lithium-Metal-Compatible High-Dielectric Electrolyte for Lithium-Sulfur Batteries. *Angew. Chem., Int. Ed.* **2018**, *57*, 16732.
(61) Jin, C. Q.; Zhai, P. B.; Wei, Y.; Chen, Q.; Wang, X. G.; Yang, W. W.; Xiao, J.; He, Q. Q.; Liu, Q. Y.; Gong, Y. J. Ni$(OH)_2$ Templated Synthesis of Ultrathin Ni_3S_2 Nanosheets as Bifunctional Electrocatalyst for Overall Water Splitting. *Small* **2021**, *17*, 2102097.
(62) Li, J. B.; Chen, C. Y.; Chen, Y. W.; Li, Z. H.; Xie, W. F.; Zhang, X.; Shao, M. F.; Wei, M. Polysulfide Confinement and Highly Efficient Conversion on Hierarchical Mesoporous Carbon Nanosheets for Li-S Batteries. *Adv. Energy Mater.* **2019**, *9*, 1901935.
(63) Hu, Y.; Hu, A. J.; Wang, J. W.; Niu, X. B.; Zhou, M. J.; Chen, W.; Lei, T. Y.; Huang, J. W.; Li, Y. Y.; Xue, L. X.; Fan, Y. X.; Wang, X. F.; Xiong, J. Strong intermolecular polarization to boost polysulfide conversion kinetics for high-performance lithium-sulfur batteries. *J. Mater. Chem. A* **2021**, *9*, 9771−9779.
(64) He, J. R.; Lv, W. Q.; Chen, Y. F.; Xiong, J.; Wen, K. C.; Xu, C.; Zhang, W. L.; Li, Y. R.; Qin, W.; He, W. D. Direct impregnation of SeS2 into a MOF-derived 3D nanoporous Co-N-C architecture towards superior rechargeable lithium batteries. *J. Mater. Chem. A* **2018**, *6*, 10466−10473.
(65) Li, J. B.; Xie, W. F.; Zhang, S. M.; Xu, S.-M.; Shao, M. F. Boosting the rate performance of Li-S batteries under high mass-loading of sulfur based on a hierarchical NCNT@Co-CoP nanowire integrated electrode. *J. Mater. Chem. A* **2021**, *9*, 11151−11159.

Recommended by ACS

Construction of Fe_2O_3 Nanosheet Arrays by Sulfur Doping toward Efficient Alkaline Hydrogen Evolution
Qiuyan Hao, Hui Liu, *et al.*
JANUARY 27, 2022
ACS APPLIED ENERGY MATERIALS
READ

Engineering of Amorphous Structures and Sulfur Defects into Ultrathin FeS Nanosheets to Achieve Superior Electrocatalytic Alkaline Oxygen Evolution
Zhiyu Shao, Qin Wang, *et al.*
NOVEMBER 09, 2020
ACS APPLIED MATERIALS & INTERFACES
READ

$NiSe_2$–FeSe Double-Shelled Hollow Polyhedrons as Superior Electrocatalysts for the Oxygen Evolution Reaction
Siva Kumar Ramesh, Jinkwon Kim, *et al.*
OCTOBER 27, 2021
ACS APPLIED ENERGY MATERIALS
READ

Transformation of Two-Dimensional Iron Sulfide Nanosheets from FeS_2 to FeS as High-Rate Anodes for Pseudocapacitive Sodium Storage
Yang Wu, Jun Xu, *et al.*
DECEMBER 04, 2020
ACS APPLIED ENERGY MATERIALS
READ

Get More Suggestions >

https://doi.org/10.1021/acsami.2c14282
ACS Appl. Mater. Interfaces 2022, 14, 50870−50879